



## Four-point probe geometric correction factor for isotropic cylindrical samples with non-equal probe distances

Sepideh Akhbarifar<sup>a,b,\*</sup>, Nicholas A. Mecholsky<sup>a,b</sup>, Marek Brandys<sup>a</sup>, Werner Lutze<sup>a</sup>, Ian L. Pegg<sup>a,b</sup>

<sup>a</sup> Vitreous State Laboratory, The Catholic University of America, Washington, D.C. 20064, United States

<sup>b</sup> Physics Department, The Catholic University of America, Washington, D.C. 20064, United States

### ARTICLE INFO

**Keywords:**

Geometric correction factor  
Resistivity  
Four probe measurement  
Variable probe spacing

### ABSTRACT

Resistivity of ceramics is usually measured by the DC-four-point-probe setup, which requires a geometric correction factor (GCF). We calculated a GCF for the general case of unequally spaced, in-line probes on isotropic, cylindrical specimens of variable size, radius and thickness. An analytical expression was obtained for the potential difference between the voltage probes by solving Laplace's equation. We show how the relative error of GCF varies with the number of Bessel functions and the number of extrema in them. GCF's sensitivity vis-à-vis probe distances, sample radius  $r_0$  and thickness  $d$  was studied to provide an error estimate dependent on measurement errors in those parameters. Contour plots of  $r_0 \cdot d$  provide GCF values without additional calculations, if the instrument's specifications are the same. Our GCF reproduced the final results from a commercial instrument very well. The deviation between the two results was 1.5% in our temperature range of 25°–300 °C.

### 1. Introduction

Electrical resistivity or specific electrical resistance ( $\rho$ ) is a physical property of a material, expressing how strongly the material opposes the flow of an electrical current. Electrical resistivity or its inverse, the electrical conductivity ( $\sigma$ ), is used to classify metals, semiconductors and insulators and ranges from  $10^{-8}$  to  $10^{16} \Omega \text{ cm}$  [1]. Hence measurements of resistivity are an important experimental quantity. One way to measure electrical resistivity is to apply an electric field  $E$  to a material and measure the resulting electric current. However, the sample's geometry can provide a difficult barrier to a simple calculation. The resistivity  $\rho$  of an isotropic material is defined by the ratio of the electric field and the current density  $J$  in the bulk,

$$\rho = \frac{E}{J}, \quad (1)$$

where  $\rho$  is measured in  $\Omega \cdot \text{cm}$ , the electric field in  $\text{V} \cdot \text{cm}^{-1}$ , and the current density in  $\text{A} \cdot \text{cm}^{-2}$ . Only if the geometry of an experimental setup is known, can the exact resistivity be calculated from electrostatic laws and bulk measurements of resistance. Following Ohm's law, a resistance  $R$  is deduced from the ratio of the voltage  $V$  and the current  $I$  and is a function of the geometry.

Although there are several approaches to account for the finite geometry of a sample using multiple configurations (see, for example, [2,3]), a single 4-point measurement is ubiquitous. In this configuration, an in-line four-point (4P) geometry is applied to minimize contributions from wires and/or contacts [4–6]. In 1975, the in-line four-point setup became a reference procedure of the American Society for Testing and Materials in the microelectronics industry [7]. With four electrodes in line, the inner two are used to measure a voltage drop  $V$ , while a known current is flowing between the two outer electrodes. The resistance  $R$  is then  $V/I$ , with the impedance of the voltage meter considered to be infinite. The resistivity of an isotropic half-space measured with four equally spaced electrodes aligned along a straight line as given by Valdes [8] may be written as a function of these applied and measured quantities:

$$\rho_{3D}^{\text{line}} = 2\pi s \frac{V}{I}, \quad (2)$$

where  $s$  is the distance between the probes.

For finite isotropic samples where the probes are located close enough to a boundary of a sample or where the thickness of the material might have an effect, Eq. (2) needs a correction factor due to geometry:

\* Corresponding author at: Vitreous State Laboratory, The Catholic University of America, Washington, D.C. 20064, United States.

E-mail address: [sepideha@vsl.cua.edu](mailto:sepideha@vsl.cua.edu) (S. Akhbarifar).

$$\rho = F \frac{V}{I} \quad (3)$$

$F$  is a geometric correction factor, which is usually split into several different factors that take into account the different effects geometry can have on the result, see Ref. [9] for a nice review. Formally,  $F$  has the dimension of a length (compare Eqs. (2) and (3)). Many studies have been published to evaluate the correction factors for different geometric configurations and probe arrangements, but not yet explicitly for non-equidistant probes inline as is the case for the device we are using. Several mathematical approaches have been used, such as the method of images [8,10–12], conformal mapping theory [13–15], solving Laplace's equations [16,17], the expansion of the Euler–Maclaurin series [18], and numerically with the finite element method [19] for computing the geometric correction factor in general.

In this study, we calculate the geometric correction factor for the case where the four probes are in line but not all equally spaced to measure resistivities of isotropic cylindrical specimens of variable sizes and thicknesses. A sensitivity analysis of the correction factor is also provided. Convergence issues are addressed and, for the work to be of general use, the Bessel extrema have been computed.

## 2. Geometric correction factor

Commercial instruments for simultaneous measurement of resistivities and Seebeck coefficients are typically equipped with proprietary software that computes a correction factor for the specific sample geometry and the positioning of the probes supplying the electrical current and for the voltage probes. For our instrument, which was built in-house, a geometric correction factor (GCF) was needed and calculated starting with the mathematical background published by Kelekanjeri and Gerhardt [20] for four probes. The accuracy of our GCF was then tested by applying it to raw data measured on the same sample with our instrument and with a commercial instrument. Additionally, the analytic solution affords us the opportunity to test the sensitivity of the GCF with respect to some of the variables of the overall geometry or placement of the probes.

Kelekanjeri and Gerhardt [20] calculated geometric correction factors (GCF) for in-line four-point (4P) measurements and arbitrary placement of the four probes on finite cylindrical specimens; at a distance  $L$  from a specimen center normal to a radius or at a distance  $L$  from a specimen center along the radius. The authors of [20] obtained an analytical expression for the potential difference between the voltage probes by solving the Laplace equation, using the separation of variables technique. The correction factor depends on the specimen radius and thickness, and on the placement of the probes.

In Ref. [20] the specimen is an isotropic uniform solid cylinder of radius  $r_0$ , thickness  $d$  and of electrical conductivity  $\sigma$ . Cylindrical

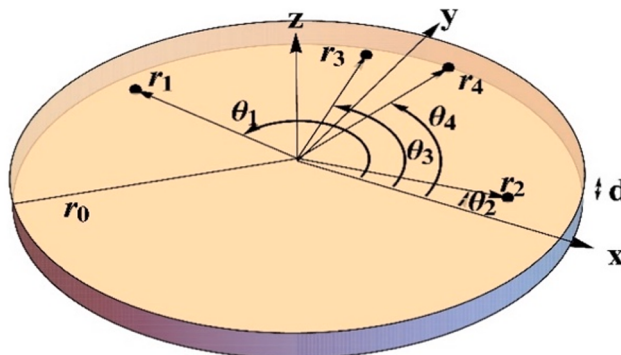


Fig. 1. Schematic showing a cylindrical specimen of radius  $r_0$  and thickness  $d$ , the location of four probes using cylindrical coordinates  $(r_i, \theta_i, 0)$  and  $i = 1, 2, 3, 4$ , on the circular face.

coordinates,  $(r, \theta, z)$ , were used to denote the location of the four-probe contacts. General probe positions (defined in Fig. 1) are indicated by  $(r_i, \theta_i, 0)$  and  $i = 1, 2, 3, 4$ . Without loss of generality, the subscripts '1' and '2' refer to two opposite current source probes ( $I_0$ ), whereas '3' and '4' refer to the voltage measurement points. The potential distribution  $\varphi(r, \theta, z)$  inside the specimen is obtained by solving Laplace's equation in this geometry, written as

$$\nabla^2 \varphi(r, \theta, z) = 0. \quad (4)$$

The source- and boundary conditions are written as follows:

$$\left( \frac{\partial \varphi}{\partial z} \right)_{z=0} = \frac{I_0}{\sigma r} (\delta(r - r_1)\delta(\theta - \theta_1) - \delta(r - r_2)\delta(\theta - \theta_2)) \quad (5)$$

$$\left( \frac{\partial \varphi}{\partial z} \right)_{z=-d} = 0 \quad (6)$$

$$\left( \frac{\partial \varphi}{\partial r} \right)_{r=r_0} = 0 \quad (7)$$

where the delta functions are at the positions of probes 1 and 2, the opposite point sources at  $(r_1, \theta_1, 0)$  and  $(r_2, \theta_2, 0)$ , respectively. The boundary conditions (7) and (8) imply that the samples' boundaries are insulating and confine the axial and radial electric fields. The solution for the potential distribution  $\varphi(r, \theta, z)$  can be achieved by separation of variables in the variables  $r$  and  $\theta$  [21–23],

$$\varphi(r, \theta, z) = \psi(r, \theta)Z(z). \quad (8)$$

By inserting Eq. (8) into the expanded Laplace's Eq. (4) and solving it, the general solution ([21]) for  $\varphi(r, \theta, z)$  is:

$$\varphi(r, \theta, z) = J_m(kr) (\sin(m\theta) + C_3 \cos(m\theta)) \times (C_1 \exp(-kz) + C_2 \exp(kz)), \quad (9)$$

where  $J_m$  is  $m$ th order Bessel function of the first kind. An explicit solution for Eq. (9) can be obtained by determining the separation constants and coefficients satisfying the source and boundary conditions (5, 6, and 7). Applying the boundary condition (7) to Eq. (9) yields:

$$\left( \frac{dJ_m(kr)}{dr} \right)_{r=r_0} = 0. \quad (10)$$

Eq. (10) is the criterion identifying the maxima or minima of  $J_m(x)$ . This equation has an infinite set of roots given by  $k_{mn} = \frac{\beta_{mn}}{r_0}$ , where  $\beta_{mn}$  ( $n = 1, 2, 3, \dots$ ) is a node corresponding to a maximum or a minimum of  $J_m(x)$  and can be tabulated once and for all (we calculate these in Ref. [24], see Section 2.3).

By using the integer values for  $m$  and positive values for  $n$  and noting the symmetry of Bessel functions [23],  $J_{-m}(x) = (-1)^m J_m(x)$ , one can find that the nodes corresponding to the maxima or minima of  $J_{-m}(x)$  are the same as those of  $J_m(x)$ . Therefore,  $k_{pn} = k_{mn}$ , with  $p = -m$ . The final expression for the solution for  $\varphi(r, \theta, z)$  is given in Ref. [20].

For a four-probe measurement, the specimen's electrical conductivity  $\sigma = 1/\rho$  is related to the deduced resistance  $R$  by the GCF (Eq. (3)), as follows [25]:

$$[GCF] = \frac{1}{R\sigma} = \frac{I_0}{\sigma \Delta \varphi_{3,4}}, \quad (11)$$

where  $I_0$  is the source current and  $\Delta \varphi_{3,4}$  is the potential difference given in Eq. (9). The GCF accounts for the finite specimen geometry as well as the arrangement (e.g., collinear or square) and the placement of the four-probe array. The GCF in Eq. (11) has the units of a length and in our work the GCF is expressed in millimeters.

## 2.1. Calculating a geometric correction factor for our instrument

Our instrument was built to hold cylindrical specimens with radius  $r_0$  and thickness  $d$  to measure resistivities. The radius  $r_0$  of the sample can either be 13 mm or 32 mm. Taking variable sample thicknesses into account is mandatory for experimental reasons: 1) Cold-pressing chemically different powders yields samples of slightly different thickness, depending on hardness, elasticity, grain size distribution, density, etc. 2) A smaller effect compared to that from cold pressing is due to shrinkage during high-temperature solid state synthesis. This affects the radius as well. A new GCF will need to be calculated for each of these eventualities.

**Fig. 2** is a schematic representation of the in-line four-point (4P) measuring device. As with commercial instruments, ours can measure electrical resistivity and the Seebeck effect consecutively as a function of temperature. Two small copper heaters (1) and (2) can generate a small temperature gradient across the sample in both directions, which is used to create the Seebeck effect. The temperature reaches from room temperature to 300 °C. Measurements can be conducted in a vacuum or under flowing inert gases. The instrument has a circular sample holder. The sample holder has two current (E1, E2) and two voltage probes (Tc1, Tc2).

A sample rests on two small copper blocks (1 and 2) with two heaters inside (H1 and H2), shown in **Fig. 2**. The gap between the sample and the heaters in **Fig. 2** was drawn only to indicate that the four probes are spring-loaded, pushing from below against the sample for good contact. Therefore, the sample must be pushed down by the spring-loaded piston, shown in **Fig. 2**.

**Fig. 3** shows the arrangement of the probes, the placement of a sample, and the spacings  $s_1$  and  $s_2$ . The sample is in contact with the small copper blocks with heaters inside (1) and (2) during measurement. The two thermocouples with their wires (yellow and green) and the current probes (red) are shown as well. The two inner electrodes (Ni-Cr) measured the Seebeck effect. The current probes are made of silver. All measurements were conducted in flowing argon. To measure resistivity,

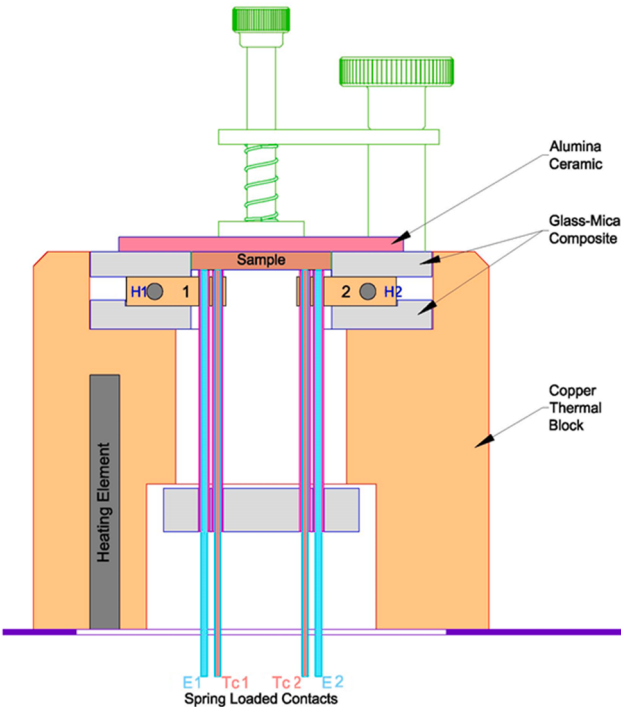


**Fig. 2.** The schematic of our 4-probe measuring device (H1, H2 are heating elements, 1,2 are copper blocks, E1, E2 are current probes, Tc1, Tc2 are voltage probes).

both outer electrodes provide a current (positive and negative) to the sample and the voltage is measured between the two thermocouples. The electrical resistivity can be calculated with Eq. (3) ( $F = \text{GCF}$ ):

$$\rho = \text{GCF} \times \frac{\Delta V}{\Delta I}, \quad (12)$$

where  $I$  is the current,  $V$  is the voltage, and GCF is the geometric correction factor, which we calculated for the cylindrical geometry of the samples.

**Fig. 4** shows a cylindrical specimen of radius  $r_0$ , thickness  $d$  and the position vectors of the current probes '1' and '2' and the voltage probes '3' and '4'. The spacings,  $s_1$  and  $s_2$ , between the probes are shown as well. The spacings are  $s_1 = 1.03$  mm and  $s_2 = 3.53$  mm and is set by the measurement device. Thickness  $d$  was about 1.5 mm to 3.5 mm for most samples.

In this case  $r_1, r_2, r_3, r_4, \theta_1, \theta_2, \theta_3$ , and  $\theta_4$  are as follows (using the coordinate system in **Fig. 1**):

$$\begin{aligned} r_1 &= s_1 + \frac{1}{2}s_2 & \theta_1 &= \pi \\ r_3 &= \frac{1}{2}s_2 & \theta_3 &= \pi \\ r_4 &= \frac{1}{2}s_2 & \theta_4 &= 0 \\ r_2 &= \frac{1}{2}s_2 + s_1 & \theta_2 &= 0 \end{aligned} \quad (13)$$

By knowing that the spacings  $s_1$  and  $s_2$  are 1.03 and 3.53 mm, respectively, then  $r_1 = r_2 = 2.795$  mm and  $r_3 = r_4 = 1.765$  mm. Since  $r_1 = r_2$ , the coefficient  $C_{40n}^*$  (in Eq. 26 of Ref. [20]) is zero for all  $n$ . The  $C_{3mn}^*$  coefficient (in Eq. 27 of Ref. [20]) is also zero because  $r_1 = r_2, \theta_1 = \pi$  and  $\theta_2 = 0$ . For even integer values of  $m$ :  $\cos(0) = 1$  and  $\cos(\pi) = -1$ , also,  $r_1 = r_2$ , therefore the  $C_{4mn}^*$  (in Eq. 28 of Ref. [20]) coefficient is zero for all even  $m$ . For odd integer values of  $m$ , the  $C_{4mn}^*$  can be written as:

$$C_{4mn}^* = -2 \frac{\alpha}{\omega_{mn}} \frac{J_m(k_{mn}(s_1 + \frac{1}{2}s_2))}{\frac{(k_{mn}r_0)^2 - m^2}{(k_{mn}r_0)^2} [J_m(k_{mn}r_0)]^2} \quad (14)$$

with

$$\alpha = \frac{2I_0}{\sigma\pi r_0^2}, \quad (15)$$

and

$$\omega_{mn} = k_{mn}[1 - \exp(-2k_{mn}d)] \quad (16)$$

Therefore, the solution for the potential can be rewritten as

$$\begin{aligned} \varphi(r, \theta, z) &= \sum_{m \neq 0} \sum_{n=1}^{\infty} C_{4mn}^* J_m(k_{mn}r) \cos(m\theta) \\ &\times (\exp[-k_{mn}(2d+z)] + \exp(k_{mn}z)), \end{aligned} \quad (17)$$

and the potential difference across the probes '3' and '4' reduces to

$$\begin{aligned} \Delta\varphi_{3,4} &= \varphi_3 - \varphi_4 = 2\varphi_3 \\ &= -2 \sum_{m \neq 0} \sum_{n=1}^{\infty} C_{4mn}^* J_m(k_{mn}r_3) (\exp[-k_{mn}(2d+z)] + \exp(k_{mn}z)), \end{aligned} \quad (18)$$

since  $r_3 = r_4, \theta_3 = \pi$ , and  $\theta_4 = 0$ , the  $\cos(m\theta)$  makes  $\varphi_3$  and  $\varphi_4$  equal in magnitude but with opposite signs and the potential difference reduces to  $2\varphi_3$ . There are infinite sums in Eq. (18), but in practice we considered  $m$  from 0 to 600 and  $n$  from 1 to 10,000 and investigated the consequences of these choices below.

We used *Mathematica* (version 10.2) to calculate  $\Delta\varphi_{3,4}$ . Then the GCF is numerically the inverse of this, using Eq. (18) with a unit conductivity in  $(1/(\Omega\text{mm}))$  and a unit current  $I_0$  (A)

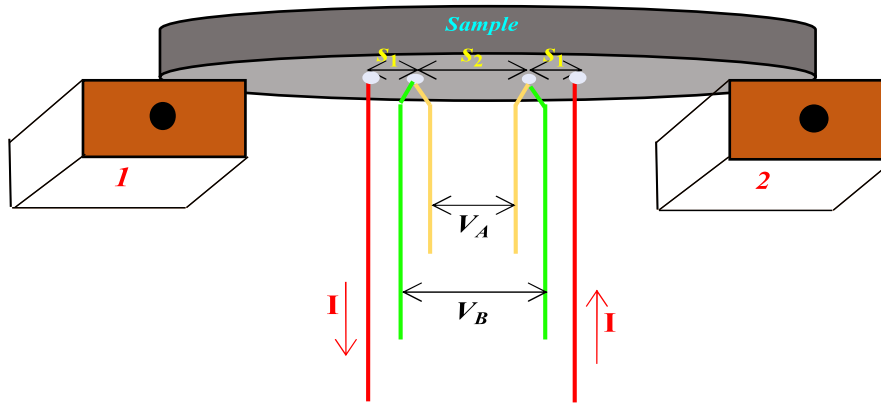


**Fig. 3.** Schematic shows four-probe setup with probe spacing. Thermocouple legs in yellow and green measure voltages  $V_A$  and  $V_B$ , current probes are red. (For interpretation of the references to colour in this figure legend, the reader is referred to the web version of this article.)

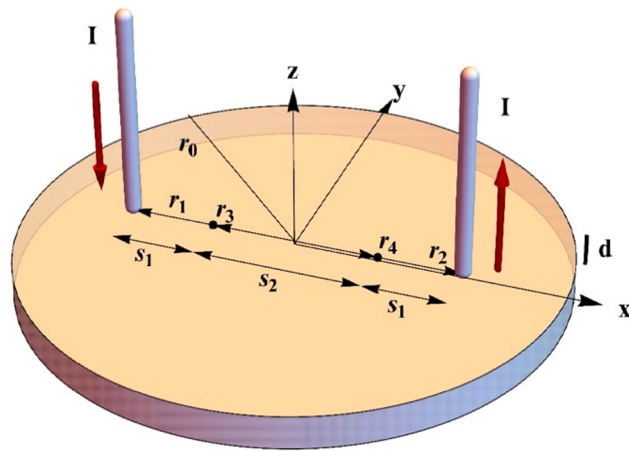


**Fig. 4.** Schematic showing a cylindrical specimen of radius  $r_0$  and thickness  $d$ , the two opposite current probe position vectors of  $r_1, r_2, r_3$ , and  $r_4$ , and the probe spacings  $s_1$  and  $s_2$ .

$$[\text{GCF}] = \frac{B}{\Delta\varphi_{3,4}}, \quad (19)$$

where  $B = \frac{I_0}{\sigma} = 1 (\text{Vm})$ . By calculating the GCF for each sample size and measuring the resistance, we can calculate the electrical conductivity ( $\text{S/mm}$ ) as follows:

$$\sigma = \frac{1}{\rho} = \frac{1}{[\text{GCF}] * R} \quad (20)$$

with  $R$  in ohms.

## 2.2. Electric potential in a cross section of the sample

**Fig. 5** shows the electric potential calculated over the sample in the  $xz$  plane using Eq. (17) with  $m = 100$  and  $n = 500$  for an isotropic material with a unit conductivity in ( $\text{S/mm}$ ) and a unit current  $I_0$  ( $\text{A}$ ) applied. The  $x$ -axis shows the diameter of the disk in mm and the  $z$ -axis is the thickness of the sample. The position vectors of  $r_1, r_2, r_3$ , and  $r_4$  as well as opposite current probes are shown in the **Fig. 5**. The curves in the interior of the cross section are contours of constant electric potential. The scale (in V) is given by in the color legend under the figure. In this figure, which is the specific case,  $r_1 = r_2 = 2.795$  mm,  $r_3 = r_4 = 1.765$  mm,  $r_0 = 16$  mm, and  $d = 2$  mm, the potential  $\varphi$  can be read from the bar scale.

## 2.3. Numerical consideration and convergence issues

In this section we provide a description for the calculation of the Bessel maxima and minima as well as some consideration given to the convergence of the results.

It is observed that the solution in Eq. (18) requires many Bessel extrema. However, there did not seem to be many tables available for the locations of the extrema for Bessel functions except Ref. [26], which provides a table for the first 6 zeros of the first 31 Bessel functions. We thus calculated 10,000 extrema for the first 601 Bessel functions using a root solver on the derivative of the Bessel function and checked against the table in Ref. [26]. These extrema are provided in Reference [24].

There were some issues to be understood in calculating the solutions in Eq. (18). To explore this to some extent, we compare solutions using different numbers of Bessel functions and extrema to determine how

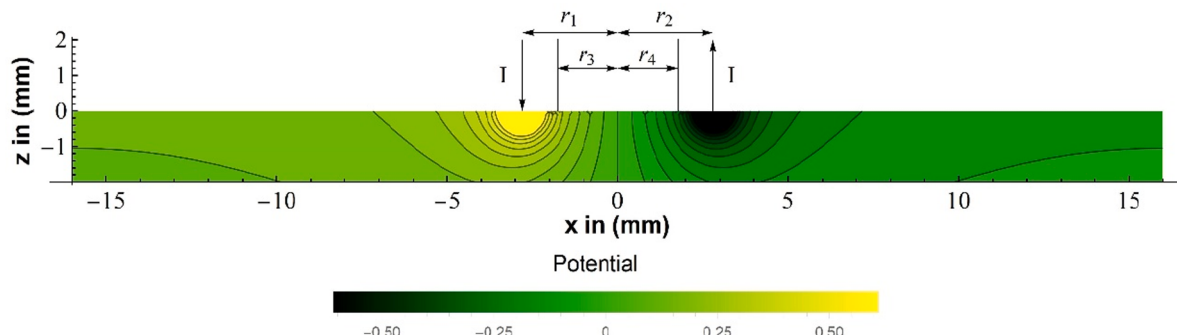


**Fig. 5.** Electric potential (in V) in a cross section of a typical cylindrical specimen of radius  $r_0 = 16$  mm, and thickness  $d = 2$  mm. The two opposite current probes, the voltage probes, and the position vectors are  $r_1 = r_2 = 2.795$  mm,  $r_3 = r_4 = 1.765$  mm, respectively.

many extrema and Bessel functions are required for a converged solution. Some of these issues were hinted in Ref. [20]. In Fig. 6, we show the contours of the relative error (compared with a maximum of 601 Bessel functions and 10,000 extrema for each Bessel function). The horizontal axis is the number of Bessel functions used and the vertical axis is the number of extrema used for each Bessel function. We see that there is oscillatory behavior with large fluctuations of the relative error with the number of extrema used. Surprisingly, the dark blue area on the upper left of the figure (using relatively few Bessel functions) represents relative errors of  $< 0.1$  ( $< 10\%$ ), as indicated by the color scale on the right side of the diagram. How can we trust a calculation that has much worse error using more Bessel functions? To better understand this behavior, we studied separately the change of the relative error with the number of Bessel functions and the number of extrema in the Bessel functions. The results are shown in Fig. 7.

In Fig. 7a, to highlight the issue, we considered 10, 50, and 100 extrema and plotted the relative error versus the number of Bessel functions. It was expected that using more Bessel functions should reduce the error when keeping the number of extrema fixed. However, using only 10 extrema (red solid curve), as we increase the number of Bessel functions, the error limits to 30%. Clearly this is unreasonable, and more extrema should be used. Accordingly, when going from 10 to 50 extrema (green dashed curve), the relative error does decrease but does not go to zero. Surprisingly, with 100 extrema (blue dot dashed curve), the final error as a function of the number of Bessel functions used (at a large number of Bessel functions) increases above the final error of 50 extrema (green dashed curve). Thus, a larger number of extrema in the Bessel functions doesn't necessarily mean better approximation. In Fig. 7b three constant numbers of Bessel functions have been chosen. We see that increasing the number of extrema makes the relative error oscillate. The values for 50 and 100 Bessel functions are the same because, as Fig. 7a shows, the error eventually converges to a specific error when there are enough Bessel functions (the individual values of Fig. 7b are the final converged values of Fig. 7a). Fortunately, we can see that the overall trend in Fig. 7b is slowly decreasing. If we choose 5 Bessel functions and increase the number of extrema up to 10000, we see that the error oscillates wildly till it eventually settles to a small relative error (in Fig. 7c). Thus, we find that a large number of extrema are needed for precise solutions. Using a large number of extrema (10000), we vary the number of Bessel functions used in (Fig. 7d). We see GCF eventually settles down to a low error, so we use  $m = 20$ ,  $n = 5000$ , for sensitivity calculations below. This was a good compromise for speed of computation.

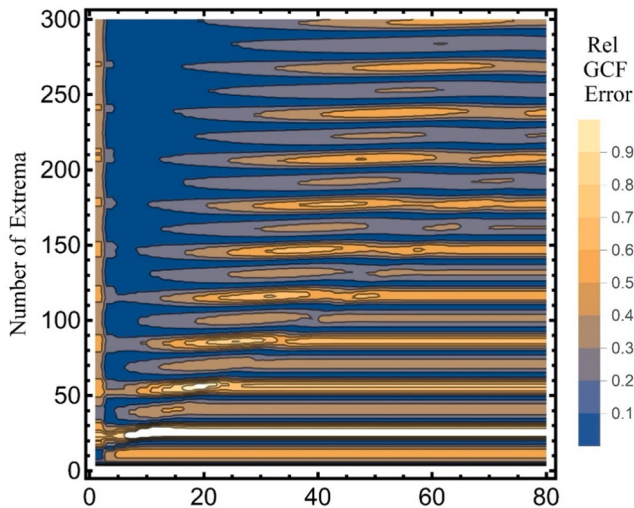


**Fig. 6.** Contours of relative error of the GCF (based on an ‘exact’ value of  $m = 600$ ,  $n = 10000$ ) as a function of the extrema order and the number of Bessel functions.

Looking back at Fig. 6, there is a minimum of error if we use combinations of extrema and the number of Bessel functions inside a wedge formed in Fig. 6 bounded by a line with a slope of approximately 15. In our work, our “exact” values are given by  $m = 600$ ,  $n = 10000$ , since this is the largest number of Bessel functions and extrema that we have within this wedge.

### 3. Verification of the geometric correction factor

The GCF of Eq. (19) was tested for accuracy. The calculated value for the GCF was 3.2 mm with the definitions mentioned above (nominal values for the instrument are  $r_0 = 16$  mm,  $d = 2.00$  mm,  $s_1 = 1.03$  mm,  $s_2 = 3.53$  mm). To test this computation, the resistivities of several of our ceramic samples (e.g., lead ruthenate,  $\text{Pb}_2\text{Ru}_2\text{O}_{6.5}$ , and some derivatives, all highly conductive pyrochlore defect structures) were outsourced and measured in the temperature range between 20° and 300 °C on Netzsch’s SBA 458 (MNEMESIS) instrument that measures resistivities and Seebeck coefficients with the in-line four-point method, like ours. According to the manufacturer Netzsch, their GCF was calculated using the finite element method. An example of an application of Eq. (20) to raw data from SBA 458 provided the result shown in Fig. 8. The blue curve (SBA 458) shows the final results of conductivity measurements on one of our samples, using SBA 458. The red curve (using our GCF) shows the final results of the same conductivity measurements but using the underlying raw data from SBA 458 and correcting them with our geometric correction factor. A comparison of the two curves in Fig. 8 shows that our GCF reproduces the final results from SBA 458 very well. The deviation between the two curves is 1.5% over the entire temperature range. The experimental standard errors based on four measurements per temperature varied with temperature and were  $\pm 0.17\%$  or less.

### 4. Sensitivity study

The geometric correction factor computed through Eq. (19) has several parametric dependences that may be investigated. Additionally, the slope of the GCF at the device’s parameter values with respect to probe separation ( $s_1$  and  $s_2$ ), radius  $r_0$ , and thickness  $d$  can be used to give an estimate of the error of the GCF using a propagation of errors technique. In this section, the sensitivity of GCF versus probe separation ( $s_1$  and  $s_2$ ), radius  $r_0$ , and thickness  $d$  is studied and shown in Fig. 9.

The four subplots in Fig. 9 show the variation of the GCF as a function of the parameters computed using Eq. (18) holding the other parameters fixed. Fig. 9a shows the variation of the GCF with respect to the probe separation  $s_1$ , Fig. 9b shows the variation with probe separation  $s_2$ , Fig. 9c with disk radius  $r_0$ , and Fig. 9d with disk thickness  $d$ . In all cases, the gray vertical lines indicate the nominal values for a typical sample in our experiment. The red sloped lines indicate numeric derivatives of the curves at these points. The numerical values of the derivatives at the nominal parameter values for the instrument ( $r_0 = 16$  mm,  $d = 2.00$  mm,  $s_1 = 1.03$  mm,  $s_2 = 3.53$  mm) are:

$$\left| \frac{\partial GCF}{\partial r_0} \right| = .11, \quad \left| \frac{\partial GCF}{\partial s_1} \right| = 2.75, \quad \left| \frac{\partial GCF}{\partial s_2} \right| = .24, \quad \left| \frac{\partial GCF}{\partial d} \right| = .55. \quad (21)$$

The computed values for the slopes are calculated from a central finite difference formula with increment  $h = 10^{-5}$  mm (the converged value for the derivatives of  $s_2$ ,  $r_0$  and  $d$ ) and  $h = 0.2$  mm for  $s_1$  (for which the error got worse at smaller values than this). One interesting feature is that the GCF is clearly more sensitive to  $s_1$  than  $s_2$ , indicating that the distance between the voltage and current probes may be an important factor in the error of the GCF in final measurements. Perkins et al. also mention this effect [2]. This may be due to the fact that  $s_1$  is the distance between the injection source and probe point. The potential changes vary rapidly in this region (as seen in Fig. 5). On the other hand, the slope is fairly constant throughout the range investigated. In the other

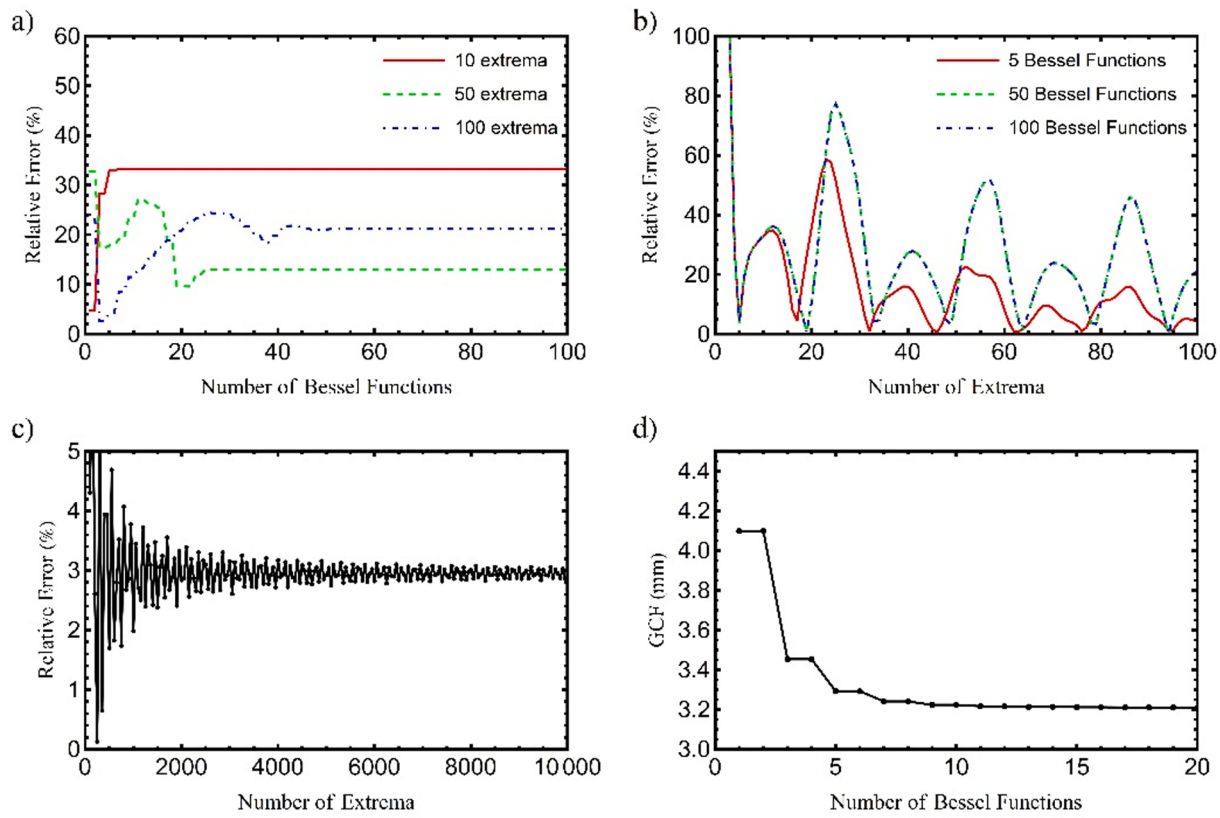


**Fig. 7.** a) Relative error vs. the number of Bessel function for 10, 50, and 100 extrema, b) Relative error vs. the number of extrema for 5, 50, and 100 Bessel functions, c) Relative error vs. the number of extrema, and d) Change of GCF with the number of Bessel functions.

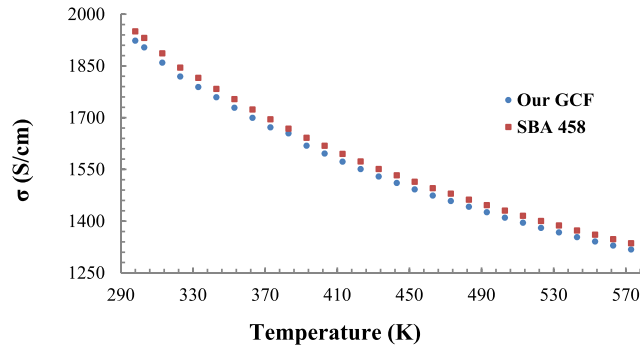


**Fig. 8.** Comparison of electrical conductivity results. Blue Data: Final results obtained with Netzsch instrument SBA 458. Red Data: Raw data from SBA 458, corrected with our GCF (Eq. (19)).

cases, the nominal parameter values are in positions of relatively shallow slopes which help the error estimate. The theoretical error based on propagation of errors is:

$$\Delta GCF = \sqrt{\left(\frac{\partial GCF}{\partial r_0}\right)^2 \Delta r_0^2 + \left(\frac{\partial GCF}{\partial s_1}\right)^2 \Delta s_1^2 + \left(\frac{\partial GCF}{\partial s_2}\right)^2 \Delta s_2^2 + \left(\frac{\partial GCF}{\partial d}\right)^2 \Delta d^2}. \quad (22)$$

For comparison, the corresponding values for the derivatives for an infinite sheet are

$$\left|\frac{\partial GCF}{\partial s_1}\right| = 2.13, \left|\frac{\partial GCF}{\partial s_2}\right| = 0.623, \quad (23)$$

and the values for the derivatives for a half space are

$$\left|\frac{\partial GCF}{\partial s_1}\right| = 4.97, \left|\frac{\partial GCF}{\partial s_2}\right| = 0.267. \quad (24)$$

For future use, one can read the GCF value from  $r_0-d$  contour plots, Fig. 10, if the instrument's specifications are the same ( $s_1 = 1.03$  mm and  $s_2 = 3.53$  mm). The contours are interpolated from a grid of GCFs calculated using  $m = 20$  Bessel functions, and  $n = 10000$  extrema with a spacing of 0.14 in the horizontal direction and 0.03 in the vertical.

## 5. Conclusions

We calculated the geometric correction factor for the general case where the four probes are in line but not all equally spaced to measure resistivities of isotropic cylindrical specimens of variable sizes and thicknesses for use in a device built to measure resistivity and the Seebeck coefficient for materials. Our calculation is based on the mathematical background provided by Kelekanjeri and Gerhardt. The expression  $\frac{1}{\Delta \varphi_{3,4}}$  (Eq. (19)) numerically determines the correction factor for the geometry of a disk. The error associated with GCF in this calculation depends on the number of Bessel functions and extrema as well as the uncertainty in the probe separation distances, thickness, and radius of the disk. Since tables for extrema in Bessel functions are not generally available, we calculated 10,000 extrema for the first 601 Bessel functions using a root solver on the derivative of the Bessel function and provide this information in reference [24]. We studied separately the change of the relative error of the GCF with the number of Bessel functions and the number of extrema used in the computation. The result was that a larger number of extrema in the Bessel functions doesn't necessarily mean better approximation (as measured by a smaller relative error). We show that the relative error becomes constant at a reasonably low value of about 3.2% when using 10 to 20 Bessel functions and a large number of extrema (10000).

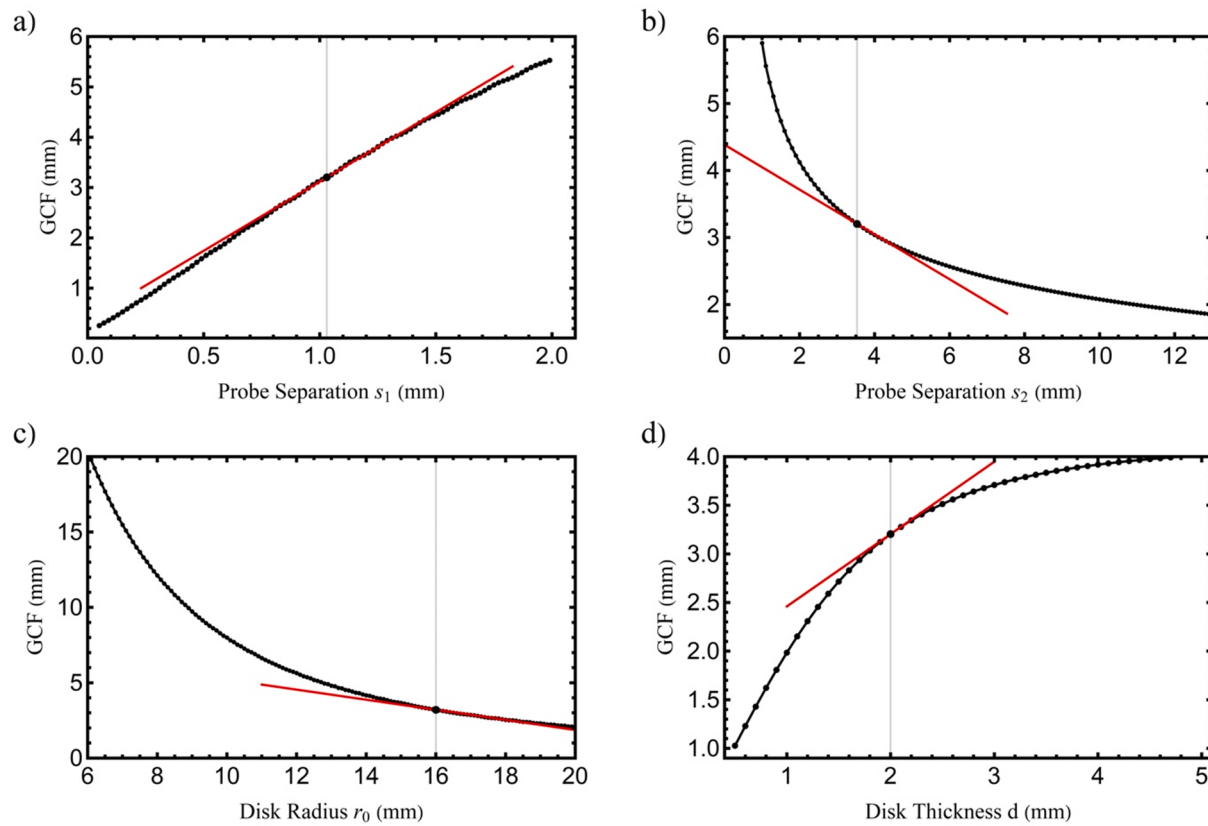


**Fig. 9.** GCF changes versus a) probe spacing  $s_1$ , b) probe spacing  $s_2$ , c) disk radius  $r_0$ , and d) disk thickness  $d$ .

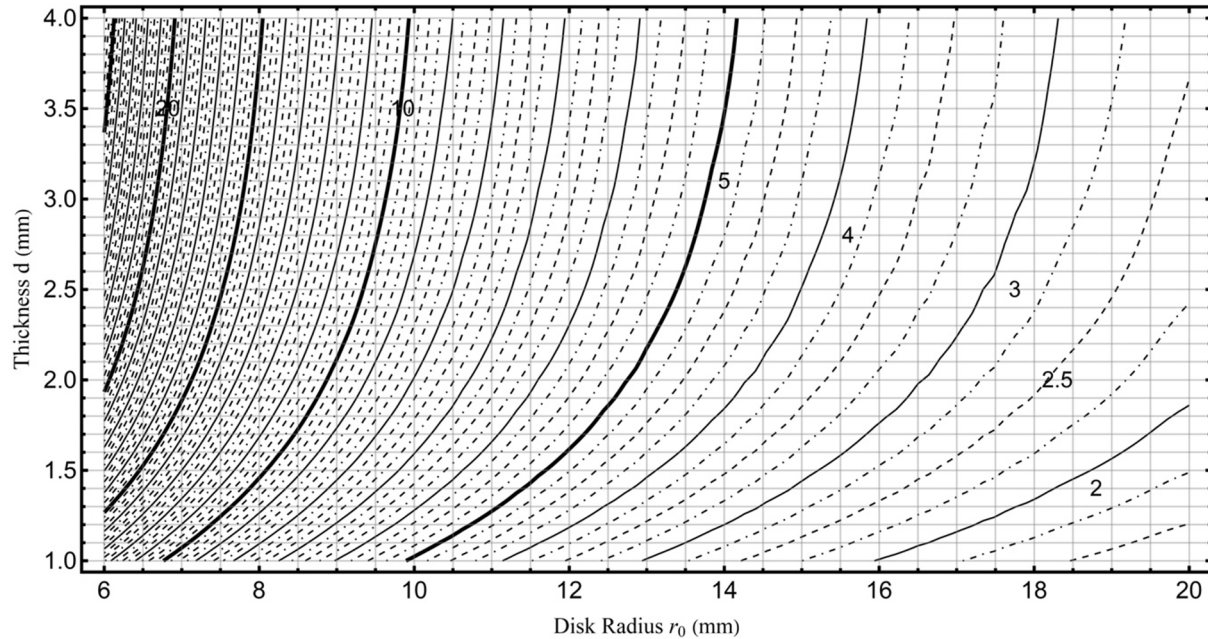


**Fig. 10.** GCF (in mm) for different disk thickness and radius ( $s_1 = 1.03$  mm and  $s_2 = 3.53$  mm) using  $m = 20$  Bessel functions, and  $n = 10000$  extrema.

The GCF was tested for accuracy. Samples of lead ruthenates were measured on a commercial instrument (Netsch's SBA 458) and the raw resistance data were corrected with our GCF and the results compared with the final results obtained from Netsch instrument. The difference between two sets of final results was 1.5% over the entire temperature range (25–300 °C).

The sensitivity of GCF versus probe separation ( $s_1$  and  $s_2$ ), radius  $r_0$ , and thickness  $d$  was analyzed and provide a measure of the uncertainty of the resulting calculation of the GCF with respect to the parameters of the radius of the disk,  $r_0$ , the thickness of the disk,  $d$ , and the probe separation parameters,  $s_1$ , and  $s_2$ . It was found that the linear coefficients for the expression of the error terms, from propagation of the

errors, are 0.11, 0.55, 2.75, and 0.24, respectively. A contour plot of  $r_0$ - $d$  was created to provide GCF values, if the instrument's specifications are the same and provide a quick way to find a GCF value without having to compute the expression.

The general method of analysis would be suited for other geometries (like a square or rectangular thin disk) where the solutions would be sines and cosines instead of Bessel functions. Additionally, the sensitivity analysis would bring interesting comparisons for the optimal geometry for measurements to minimize the GCF error.

### CRediT authorship contribution statement

**Sepideh Akhbarifar:** Conceptualization, Data curation, Formal analysis, Writing – original draft, Validation, Visualization. **Nicholas A. Mecholsky:** Conceptualization, Data curation, Formal analysis, Writing – original draft, Validation, Visualization. **Marek Brandys:** Methodology. **Werner Lutze:** Supervision, Writing – review & editing. **Ian L. Pegg:** Writing - review and editing, Funding acquisition.

### Declaration of Competing Interest

The authors declare that they have no known competing financial interests or personal relationships that could have appeared to influence the work reported in this paper.

### Acknowledgement

The authors would like to thank an anonymous reviewer for the calculations in Eq. (23) and Eq. (24).

### References

- [1] R.A. Serway, Principles of Physics, Saunders College Publishing, London, 1998, p: 602.
- [2] E. Perkins, L. Barreto, J. Wells, P. Hofmann, Surface-sensitive conductivity measurement using a micro multi-point probe approach, *J Rev. Sci. Instrum.* **84** (2013), 033901.
- [3] S. Thorsteinsson, F. Wang, D.H. Petersen, T.M. Hansen, D. Kjær, R. Lin, J.-Y. Kim, P.F. Nielsen, O. Hansen, Accurate micro four-point probe sheet resistance measurements on small samples, *J Rev. Sci. Instrum.* **80** (2009), 053902.
- [4] F. Wenner, A method of measuring earth resistivity, *Bull. Bur. Stand.* **12** (1916) 469–478.
- [5] M.A. Logan, An AC bridge for semiconductor resistivity measurements using a four-point probe, *Bell Syst. Technol. J.* **40** (1961) 885–919.
- [6] L.J. Swartzendruber, Four-point probe measurement of non-uniformities in semiconductor sheet resistivity, *J. Solid-State Electron.* **7** (1964) 413–422.
- [7] ASTM 1975 Annual Book of ASTM Standards part 43, F84.
- [8] L.B. Valdes, Resistivity measurements on germanium for transistors, *Proc. IRE* **42** (1954) 420–427.
- [9] I. Miccoli, F. Edler, H. Pfünf, C. Tegenkamp, The 100<sup>th</sup> anniversary of the four-point probe technique: the role of probe geometries in isotropic and anisotropic systems, *J. Phys. Condens. Matter.* **27** (2015), 223201.
- [10] F. Keywell, G. Dorosheski, Measurement of the sheet resistivity of a square wafer with a square four-point probe, *Rev. Sci. Instrum.* **31** (1960) 833.
- [11] F.M. Smits, Measurement of sheet resistivities with the four-point probe, *Bell Syst. Tech. J.* **37** (1958) 711–718.
- [12] M.G. Buehler, W.R. Thurber, Measurements of the resistivity of a thin square sample with a square four-probe array, *Solid-State Electron.* **20** (1977) 403–406.
- [13] A. Mircea, Semiconductor sheet resistivity measurements on square samples, *J. Sci. Instrum.* **41** (1964) 679.
- [14] J.D. Wasscher, Electrical transport phenomena in MnTe, an antiferromagnetic semiconductor, *Technische Hogeschool, Eindhoven*, 1969.
- [15] W. Versnel, Electrical characteristics of an anisotropic semiconductor sample of circular shape with finite contacts, *J. Appl. Phys.* **54** (1983) 916.
- [16] S.Z. Tehrani, W.L. Lim, L. Lee, Correction factors for films resistivity measurement, *J. Meas.* **45** (2012) 219–225.
- [17] J. Albers, H.L. Berkowitz, An alternative approach to the. Calculation for four-probe resistances on nonuniform structures, *J. Electrochem. Soc.* **132** (2453) (1985).
- [18] R.A. Weller, An algorithm for computing linear four-point probe thickness correction factors, *Rev. Sci. Instrum.* **72** (2001) 3580.
- [19] J. Shi, Y. Sun, New method of calculating the correction factors for the measurement of sheet resistivity of a square sample with a square four-point probe, *Rev. Sci. Instrum.* **68** (1997) 1814.
- [20] Kelekanjeri V. Siva, G. Kumar, R.A. Gerhardt, A closed-form solution for the computation of geometric correction factors for four-point resistivity measurements on cylindrical specimens, *Meas. Sci. Technol.* **19** (2008), 025701.
- [21] W.N. Cottingham, D.A. Greenwood, *Electricity and Magnetism*, Cambridge University Press, New York, 1991.
- [22] E. Kreyszig, *Advanced Engineering Mathematics*, Wiley Eastern, New Delhi, 1994.
- [23] H.J. Weber, G.B. Arfken, *Essential Mathematical Methods for Physicists*, Elsevier, San Diego, CA, 2004.
- [24] N.A. Mecholsky, S. Akhbarifar, W. Lutze, M. Brandys, I.L. Pegg, Bessel function extrema to 600 orders and 10000 extrema, *Data in Brief*, submitted, 2021.
- [25] H. Topsoe, Geometric correction factors in four-point resistivity measurement, *Bulletin No. 472-13, Haldor Topsoe – Semiconductor Division, Vedbaek*, 1968.
- [26] K.W. Andrews, A table of maxima and minima of the Bessel functions  $J_n(Z)$  for  $n=0$  to  $n=30$ , *Acta Crystallograph. Section A: Crystal Phys., Diffraction, Theor. General Crystallogr.* **37** (1981) 765–766.